ELSEVIER

Marine Geology 187 (2002) 347–363

MARINE GEOLOGY
INTERNATIONAL JOURNAL OF MARINE GEOLOGY, GEOCHEMISTRY AND GEOPHYSICS

www.elsevier.com/locate/margeo

Mechanical response of sediments to bubble growth

Bruce D. Johnson [a,*], Bernard P. Boudreau [a,b], Bruce S. Gardiner [a], Regine Maass [a]

[a] Oceanography Department, Dalhousie University, Halifax, NS, Canada B3T 1S6
[b] Southampton Oceanography Centre, University of Southampton, Waterfront Campus, European Way, Southampton SO14 3ZH, UK

Received 23 February 2001; accepted 13 May 2002

Abstract

Modeling the process of bubble growth in sediments requires an understanding of the physics that controls bubble shape and the interaction of the growing bubble with the sediment. To acquire this understanding we have conducted experiments in which we have injected gas through a fine capillary into natural and surrogate sediment samples and have monitored pressure during bubble growth to provide information about stress and strain. In gas injection studies with natural sediment samples, we have observed two modes of bubble growth behavior. One of these modes, characterized by a saw-tooth record of pressure as the bubble grows, is consistent with fracture of the medium. Observations indicate that bubble growth by fracture should correspond to bubbles that are coin- or disk-shaped. This shape is confirmed in observations of bubbles in natural sediments and in our studies of bubble injection into gelatin, a surrogate sediment material. Interpretation of the stress–strain results for bubble growth also required that we measure Young's modulus, E. The measurements show E to be near 0.14 MN m^2, which differs by more than 4 orders of magnitude from values that have been reported in the literature. Our measurements of E give substantially better estimates of bubble shape than are predicted using the literature values. Our data are interpreted with linear elastic fracture mechanics (LEFM) which predicts that the critical pressure for bubble growth will depend on the bubble volume, V raised to the $-1/5$ power. While evidence of substantial heterogeneity in sediment properties is apparent in our results, this $V^{-1/5}$ dependence is confirmed. Through application of LEFM theory, we have determined the critical stress intensity factor, K_{1c}, a material property and the principal determinant of bubble shape and growth by fracture. Our values of K_{1c} range from $\sim 2.8\times10^{-4}$ MN m$^{-3/2}$ to $\sim 4.9\times10^{-4}$ MN m$^{-3/2}$ for our natural sediment samples from Cole Harbor, Nova Scotia. We have also estimated the critical stress intensity factor for Eckernförde Bay samples by analyzing published images of natural bubbles. The K_{1c} obtained in this way is similar to our Cole Harbor results and is $\sim 5.5\times10^{-4}$ MN m$^{-3/2}$.

Keywords: methane bubbles; sediment fracture; bubble growth; sediment properties

---

1. Introduction

Understanding the growth of bubbles in aqueous sediments is important because these bubbles act as acoustic reflectors (e.g., Judd and Hovland, 1992), destabilize structures that rest on the bottom (Wheeler, 1988), and transport methane, a potent greenhouse gas, to the atmosphere (Crill et al., 1991). While there has long been an under-

---

[*] Corresponding author. Fax: +1-902-852-4433.
E-mail address: bjohnson@is.dal.ca (B.D. Johnson).

PII: S0025-3227(02)00383-3

standing of the chemical and biological processes that produce methane in sediments (e.g., Martens and Berner, 1974), the physics of bubble growth and the coupling of this growth to methane production and transport are only now being investigated.

Field observations have shown that bubbles form in organic-rich sediments on annual time scales (Strayer and Tiedje, 1978; Martens and Klump, 1980; Chanton et al., 1989). Methane production and bubble growth are particularly active when sediments are warmed in summer and enriched with organic matter from the spring bloom. At the end of summer the ebullitive flux through the sediment–water interface reaches a peak. This annual time scale for bubble growth, driven by natural rates of methane production and mass transfer, has recently been confirmed through modeling (Boudreau et al., 2002). The model, unique in featuring a distributed source of gas for bubble growth, predicts rates of bubble production that match observed rates for three different marine sites.

A model for bubble growth in sediments requires information on real bubble shape and on the physics of interaction of the growing bubble with the medium. In the absence of definite information on either of these bubble growth characteristics, Boudreau et al. (2002) assumed a spherical bubble shape, and a simple viscous interaction of the growing bubble with the sediment matrix. While inclusion of other shapes and more complex medium interaction is not expected to invalidate the conclusions of Boudreau et al. (2002), there are applications where greater accuracy is important, e.g., in acoustics or in modeling of bubble movement. To provide this greater accuracy, we have investigated the physics of bubble growth in natural and surrogate sediment materials, and we plan to integrate the results of this study into a transport–reaction model in a subsequent publication.

There is evidence to suggest that bubbles in sediments are not generally spherical. In a study of bubbly sediments in Eckernförde Bay (Abegg et al., 1994), core samples maintained at in situ pressure were scanned using X-ray tomography. The resulting images showed that bubbles are often coin- or disk-shaped with their long axis oriented vertically. The sizes of these coin-shaped bubbles were as much as ~2.5 cm in their longest dimension.

In order to better understand the dynamics of the growth of bubbles and the evolution of their shapes, we have studied bubbles produced in the laboratory in natural and surrogate sediment samples. In particular, we have injected gas through a fine capillary into natural and surrogate (gelatin) samples, and have followed gas pressure to provide information on stress and strain during bubble growth. Our experiments are designed to determine how sediment properties influence bubble shape and growth rate, and to examine the effect on growth of the heterogeneity of sediment properties at space scales appropriate to bubbles in natural sediments.

2. Experimental

Sediment samples were collected on November 4, 1999 at low tide in less than 1 m of water at Cole Harbor, Nova Scotia, Canada. To collect these samples, 31-cm-long pieces of core liner (5.6 cm internal diameter) were pushed at least 20 cm into the bottom. The upper cap was then affixed while the liner was in the sediment, and then the liner with sample inside was pulled out of the bottom. Care was taken to ensure minimum sample disturbance during the procedure. Once the tube with sample was clear of the bottom, the lower endcap was affixed, and both caps were taped in place around the periphery of the liner. The core samples collected in this manner were transported back to the laboratory in ice and then stored until use by immersion in a bucket filled with coastal seawater in a cold room maintained at ~5°C.

The apparatus for gas injection, shown in Fig. 1, consisted of a gear motor, a piston and cylinder arrangement for delivering gas, and a platform with a capillary (2 cm long and 0.1 cm inside diameter at the tip) secured through its center. Inside the capillary was a small-diameter (0.08 cm) stainless steel wire that reached the capillary tip. The other end of this wire went into a sidearm

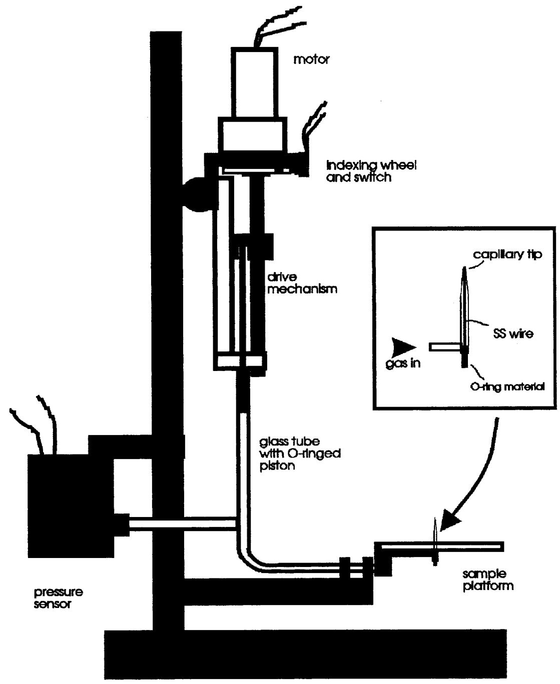

Fig. 1. The apparatus for injecting bubbles into samples of sediment and gelatin. In operation, the gear motor is activated for one full turn (controlled by an indexed wheel and switch), causing a threaded rod to move the piston and thereby reduce the volume of the injection system by 0.00359 cm^3. Gas is injected into samples through a capillary with 0.05 cm inside diameter. Inside the capillary is a small-diameter (0.03 cm) stainless steel wire that reaches the capillary tip. The other end of this wire enters a sidearm of the glass tube and is imbedded in a piece of O-ring material that is forced into the sidearm opening to provide a seal. By pressing on the bottom of the O-ring material, the wire can be moved vertically to clear the tip of the capillary. A highly accurate and sensitive pressure sensor (Paroscientific) communicates with the gas injection system through another side arm, and measures the pressure inside the bubble during the injection experiment.

of the glass tube and was imbedded in a piece of O-ring material that had been forced into the sidearm opening to provide a seal. By pressing on the bottom of the O-ring material, the wire could be moved vertically to clear the tip of the capillary.

To control delivery of gas through the capillary, the apparatus was fitted with an indexed metering wheel and switch that stopped the piston drive mechanism after one complete turn of the motor. This arrangement allowed precise delivery of the same small volume increment of gas each time the motor was activated.

A highly accurate and precise pressure sensor (Paroscientific; 0.02% $year^{-1}$ accuracy, microbar precision) with a 30-psi full scale range was placed in the gas line between the piston and the platform. This sensor measured the pressure of the gas in the system and hence the pressure in the bubble.

To begin an experiment, a section of core approximately 6 cm long was cut with a bandsaw. The cut end of the sample was then sealed with plastic wrap that was taped around the periphery of the liner tube. The sample was then carefully placed on the platform in a manner in which the capillary penetrated the plastic wrap and entered the sediment. When the sample rested on the platform, the capillary tip was located inside the sediment ~2 cm above the sample bottom. Prior to injection of gas, the stainless steel wire was pushed several times to ensure that the capillary tip was clear. During the experiment, pressure was measured at 2-s intervals, with the first measurements made before the capillary was inserted. All readings were stored on a computer.

In operation, the gear motor was activated, turning a threaded rod (12.6 threads cm^{-1}) one full turn. This turn drove a threaded aluminum piece down a guide channel, which forced the piston ahead and in so doing reduced the volume of the injection systems by 0.00359 cubic centimeters. Each activation of the motor took 5 s to complete a full turn, and an interval of ~80 s elapsed between successive activations of the motor. This time interval, controlled by a timer circuit, allowed a short period for the bubble/sediment system to respond to each increment of gas delivery. However, experiments with other time intervals have shown that the duration of the interval is not critical to bubble growth behavior.

We have chosen to grow bubbles through small increments of gas delivery in order to obtain information about bubble volume. When the experiment is conducted with natural sediments the bubble size is not readily observable. This is a problem, because during an experiment the bubble may shrink or grow due to mass transfer, or in some cases, buoyancy may cause part of the bubble to separate from the capillary tip. By growing the bubble with known increments of gas addition, the bubble volume can be estimated from the pressure change that results from the volume perturbation.

For this volume perturbation method we assume ideal gas behavior, i.e., $PV=nRT$, in which n is number of moles of gas, R is the gas law constant, and T is absolute temperature. The total differential is then:

$$\mathrm{d}P = \frac{\partial P}{\partial V}\mathrm{d}V + \frac{\partial P}{\partial n}\mathrm{d}n + \frac{\partial P}{\partial T}\mathrm{d}T \tag{1}$$

Assuming that the first term on the right is much greater than the last two terms during the time in which the perturbation is actually being applied (see Appendix A for proof of this condition in our study), and evaluating $\partial P/\partial V$ using the ideal gas law, gives:

$$\frac{\mathrm{d}P}{\mathrm{d}V} = -\frac{nRT}{V^2} \tag{2}$$

Substituting P for nRT/V:

$$V = -\frac{P}{\mathrm{d}P/\mathrm{d}V} \tag{3}$$

or for small ΔV, Eq. 3 can be approximated as:

$$V = -\frac{P}{\Delta P/\Delta V} \tag{4}$$

In Eq. 4, V is the total volume of the system. Subtracting the dead volume V_d, i.e., the volume of the delivery system, gives the volume of the bubble.

$$V_\mathrm{bub} = -\frac{P_\mathrm{i}}{\Delta P/\Delta V} - V_\mathrm{d} \tag{5}$$

in which P_i is the instantaneous bubble pressure, and ΔP is the change in pressure in response to the incremental change in volume of the system (0.00359 cm^3, i.e., one rotation of the drive motor). Note that this method only applies when the bubble volume does not change during an incremental addition of gas. As will be seen, this condition appears to be met much of the time during bubble growth in our sediment samples.

A second method to estimate bubble volume assumes that the number of moles of gas in the system, i.e., the apparatus plus the bubble volume, remains constant during an experiment. If this condition is met, the product of pressure, P, and volume, V, of the system, i.e., PV, will remain constant. The bubble volume can then be determined from the initial PV divided by the instantaneous pressure of the system (minus the known dead volume, i.e., that volume of the system that does not include the bubble).

In this second method, we again assume ideal gas behavior, but further assume that the number of moles of gas in the system is invariant during an experiment, i.e., no diffusive loss. In this case:

$$V_\mathrm{bub} = \frac{(PV)_0}{P_\mathrm{i}} - V_\mathrm{d} \tag{6}$$

in which $(PV)_0$ is determined before the bubble forms at the capillary tip and is assumed to remain constant for the duration of the experiment.

There are advantages and disadvantages to each method for estimating bubble volume. For the volume perturbation method, no assumptions are made about the number of moles of gas in the system. Therefore, loss of gas through mass transfer, bubble separation or even system leaks does not introduce error into the estimate. However, for the volume perturbation method to be feasible, no change in bubble volume can accompany a particular incremental addition of gas. If the bubble expands during addition of gas, then ΔP will be small and the predicted bubble volume will be larger than the true bubble volume. In treating the data, we have set a threshold minimum for the change in pressure that accompanies incremental volume addition. This threshold removes large extraneous peaks.

The advantage of the constant PV method is that it can be applied even when conditions that govern the applicability of the volume perturbation method are violated. However, this method ignores any changes in the number of moles of gas in the system.

In addition to conducting experiments with natural sediment samples, bubbles were injected into various surrogate materials. The objective was to find a surrogate in which bubble growth could be followed visually and for which the pressure–volume behavior during growth matched that observed for natural sediment samples. The materials that were tested include: gelatin of various strengths, baby oil gel, and glycerine filled with powdered Pyrex. In this last system, the refractive index of the glycerine was modified slightly with water to match the refractive index of the Pyrex. Of these surrogates gelatin provided results most similar to bubble growth behavior in the Cole Harbor samples. Consequently, the results for gelatin and natural sediments will be described here.

To provide information on the shapes of bubbles formed from injected gas, some of the samples of the Cole Harbor sediments were X-rayed before and after gas injection. To do this, the whole apparatus was placed in an X-ray cabinet. Because of the configuration of the cabinet, images could only be made from the top of the core.

Cole Harbor sediment samples were characterized by salinity, percentage of water and percentage of organic matter. Salinity was determined by refractometer using samples of pore water. Percentage of water was obtained gravimetrically by drying approximately 10 g sub-samples of core in a drying oven at 50°C for 20 h. The percentage of organic matter was determined again gravimetrically through combusting the dried sub-samples for ~7 h at 450°C. Correction for salinity was made for both gravimetric analyses.

To interpret our bubble growth results, we also found it necessary to make experimental determinations of Young's modulus, E, for our sediment samples. These measurements were made with a simple apparatus that consisted of two acrylic platforms joined with a steel rod through a steel sleeve. The sleeve was held so that the platforms were constrained to move vertically, and the amount of this movement was gauged using a set of dial calipers that were affixed above the upper platform to measure its vertical position.

In operation, weights were added to the top platform and this stress was transmitted to the sample through the rod and the interface between the lower acrylic plate and the sample. The strain associated with the stress was then measured with the calipers. In making a measurement, a sub-sample of sediment was prepared by first cutting it on a bandsaw from one of the samples from Cole Harbor. The core liner was then cut through lengthwise in four places around the perimeter, and the core sample removed from the liner by running a fine wire down the slots of the cuts and then between the liner and sample. The result was a sediment sample ~7 cm long and 5.7 cm diameter that was little disturbed.

The sediment sample was placed on a Petri dish in contact with the underside of the lower platform. The height of the sample was adjusted such that the position of the platform was near mid-range of the travel of the rod in the sleeve. Weights from 171 g to 1146 g were added sequentially to the upper platform. The position of the platform was measured before each weight was added, and then again with the weight in place, and finally when the weight had been removed. Care was taken to remain within the elastic limit of the material.

3. Results

Fig. 2 shows an X-ray image (top view) of a core sample from Cole Harbor after injection of 0.3 ml of gas. In Fig. 2 and images of four other injections into natural samples from Cole Harbor, none showed gas inclusions to be spherical. In-

Table 1
Characterization of sediment samples collected on November 4, 1999 in terms of salinity, percentage water, and percentage organics

Core	Sample	Salinity (ppt)	Water (%)	Organics (%)
24	1	29	39.97	2.83
	2	30	27.23	1.92
	3	32	26.84	1.51
	4	32	31.22	1.52
25	1	32	29.79	2.22
	2	40	36.75	2.94
26	1	32	36.95	2.73
	2	30	29.77	2.02

The cores were collected at Cole Harbor, NS. 'Sample' refers to where in the core the sample was taken, i.e., 1 refers to the bottommost 5-cm portion. Results for percent water and percent organics have been corrected for salt content.

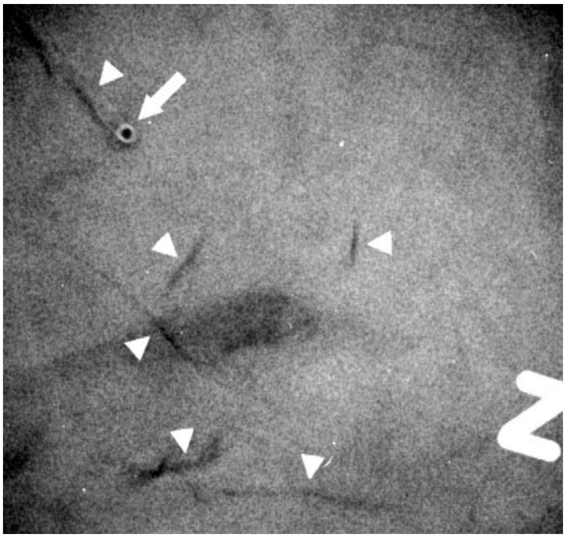

Fig. 2. X-ray image of the top of a sediment sample from Cole Harbor. The crack-shaped darker areas (arrows) identify the less dense bubble regions. The letter 'Z' was placed on the core as a marker and is made of lead. The long arrow at the top of the image shows the capillary tip and, above that, the gas that was injected from the tip.

stead, bubbles were always crack-shaped, and in one case the injected gas was observed to expand a crack that was visible in the sample prior to gas injection.

Results of analyses for salinity, water content and percentage organic matter appear in Table 1. Pore water salinities for the core samples generally ranged between 29 ppt and 32 ppt, although one of the measurements was exceptionally high at 40 ppt and is thought to be in error. The percentage of water in the samples ranged from 26.84% to 39.97%, and organics from 1.51% to 2.94%.

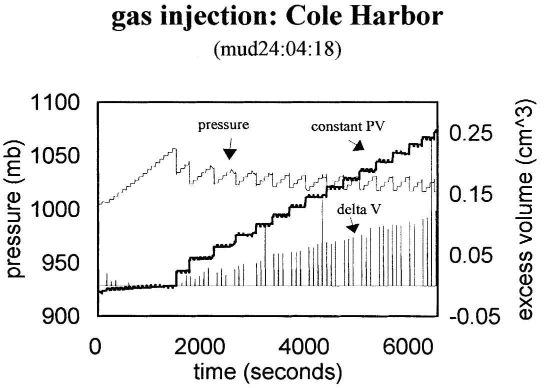

Fig. 3. The record of injection for one sample of sediment from Cole Harbor. The curves for pressure and volume determined from constant *PV*, and volume perturbation methods are noted.

The injection of gas into the sediment samples gave results for pressure versus time that are indicative of substantial heterogeneity in the material properties. However, two types of behavior are common in these results. The first is rise of pressure to a peak, followed by precipitous fall in pressure that indicates bubble formation, and then a slowly declining saw-tooth pattern as the bubble grows (Fig. 3). The second type of behavior is rise to a peak and fall, again indicative of bubble formation, and then a relatively smooth bubble growth at a pressure that is typically between the peak value and the baseline (Fig. 4). While some relatively pure examples of each of these types of behavior were obtained, many results showed a growth behavior intermediate between these two end members, i.e., sometimes saw-toothed, other times smooth, or small ampli-

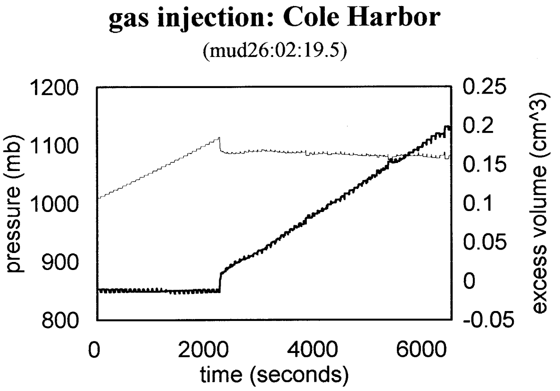

Fig. 4. The second type of behavior seen for bubble injection in Cole Harbor samples. This type of behavior shows a relatively smooth bubble growth that we interpret as local fluidization of the sediment as opposed to the saw-tooth bubble growth curve of Fig. 3 that we interpret as fracture. Only the constant *PV* method could be used to estimate bubble volume, because each incremental addition of gas resulted in an increase in bubble volume. This type of behavior violates the conditions for application of the volume perturbation method. (The heavy solid line is bubble volume determined from the constant *PV* method, and the thin solid line is the bubble internal pressure.)

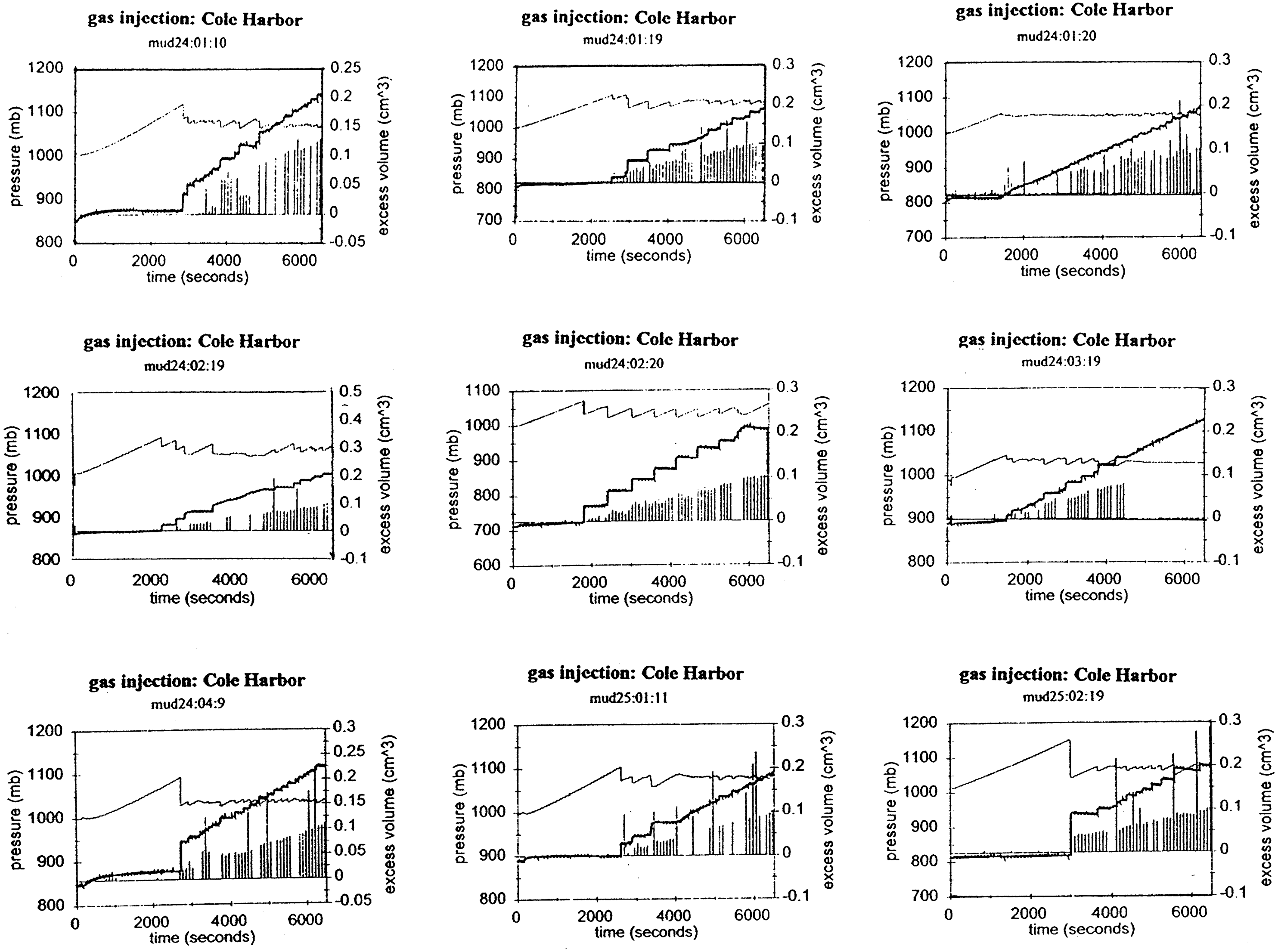

Fig. 5. Results of bubble injection into various sediment samples from Cole Harbor, Nova Scotia. Note the effect of sediment heterogeneity in the pressure curves for most of the results. (The heavy solid line is bubble volume determined from the constant *PV* method; the vertical lines show the bubble volume determined from the volume perturbation method; the thin solid line is the bubble internal pressure.)

tude saw-toothed. Some examples of bubble growth results appear in Fig. 5.

Bubble volume calculated by the two methods described previously, i.e., volume perturbation and constant *PV*, are also shown in Figs. 3 and 5. Fig. 4 shows volume calculated by the constant *PV* method only, because each increment of gas addition resulted in bubble growth, and thus the conditions for using the volume perturbation method were violated. In all cases for which we have data for both estimates of bubble volume, the constant *PV* approach predicts a larger bubble size than does the volume perturbation approach; however, the difference between the two methods is usually within a factor of 2.

The importance of making both types of estimates of bubble volume for the gas injection experiments is apparent from examination of Fig. 6. Here, the results from one injection experiment show that pressure was highly variable. Volume determined from constant *PV* shows that each time the pressure falls, the inferred volume increases. However, the volume perturbation results show that several of the pressure drops were not associated with bubble growth but, instead, indicate a volume decrease. This decrease in volume is consistent with loss of gas, as portions of the bubble separate from the capillary tip. A similar indication of gas loss appears in some of the other results of our experiments.

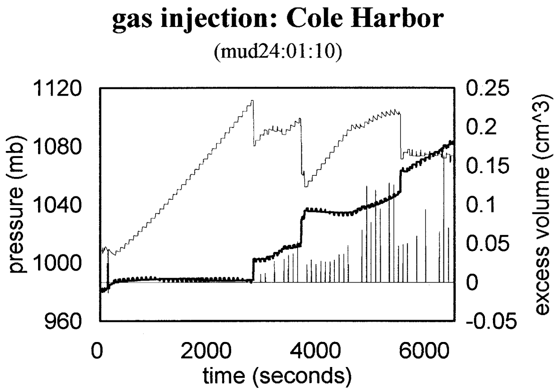

Fig. 6. Results of one injection experiment that suggest loss of gas by bubble separation from the capillary. Note that the constant *PV* approach suggests that bubble volume grows each time the pressure drops. However, the volume perturbation method indicates that, instead of growth, the bubble is actually getting smaller as portions of the bubble separate from the capillary tip. (The heavy solid line is bubble volume determined from the constant *PV* method; the vertical lines show the bubble volume determined from the volume perturbation method; and the thin solid line is the bubble internal pressure.)

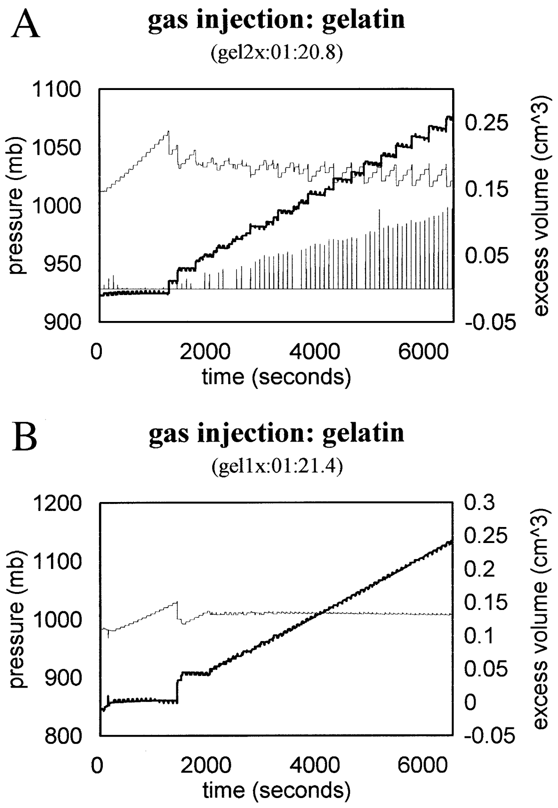

Fig. 7. Growth curves for injection of gas into (A) 2×gelatin and (B) 1×gelatin. Note the similarity to results for the sediment samples in Figs. 3 and 4. (The heavy solid line is bubble volume determined from the constant *PV* method; the vertical lines show the bubble volume determined from the volume perturbation method; and the thin solid line is the bubble internal pressure.)

Bubble growth in gelatin gave results that were similar to both types of observed behavior for sediments. For gelatin made at two times the normal strength (2×gelatin) the growth behavior (Fig. 7A) was similar to the saw-tooth pattern observed in Fig. 3, while for normal strength gelatin (1×gelatin) the result (Fig. 7B) was similar to that in Fig. 4, i.e., the nearly smooth pressure with bubble growth.

The shape of bubbles formed in gelatin was seen to be disk-like, or oblate spheroidal, with the long axis oriented vertically (Fig. 8). For 2× gelatin the bubbles were longer and thinner than those in 1× gelatin. While accurate measurement of the bubble dimensions is difficult, we have estimated aspect ratio, width to height, for bubbles in 2× gelatin and 1× gelatin to be 0.03 and 0.09, respectively.

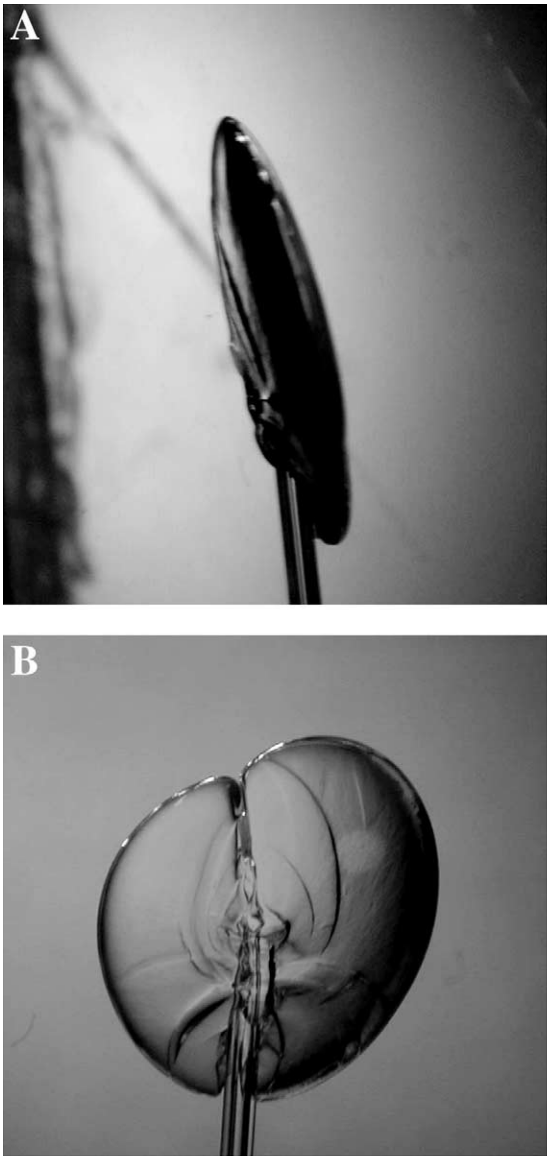

Fig. 8. Images of a bubble injected into 2× gelatin. (A) Side view. (B) Front view.

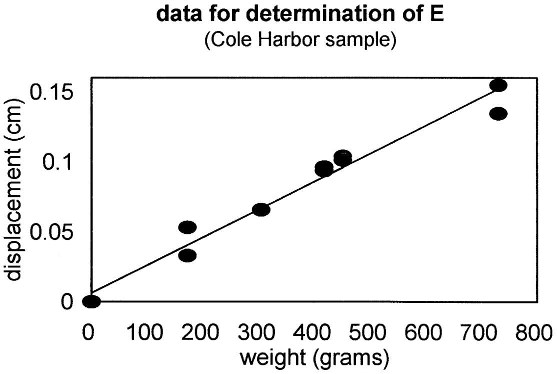

Fig. 9. Stress–strain results for two sets of measurement of Young's modulus on a Cole Harbor sediment sample.

Stress–strain results for determination of Young's modulus for a typical sediment sample from Cole Harbor appear in Fig. 9. The best fit straight line determined from regression is also shown. For this sample, the slope determined from the regression gave a Young's modulus of 0.139 MN m^{-2}.

4. Discussion

The X-ray images (top view) of Cole Harbor sediment samples showed gas inclusions to be crack-shaped (see Fig. 2). This shape is consistent with a disk on edge as observed for the shapes of bubbles of similar growth behavior formed in gelatin. Both suggest the disk- or coin-shape observed for bubbles in sediments in Eckernförde Bay (Abegg et al., 1994). The bubbles in that study were also described as being oriented with long axis oriented vertically.

While we began trying to understand bubble growth results in terms of rheological properties of the medium, we have since concluded that the observed saw-tooth pattern for bubble growth (e.g., Fig. 3) is controlled by fracture. To interpret our results, we have employed the simplest theory of fracture, the theory of linear elastic fracture mechanics (LEFM). This theory deals with materials with cracks and the stresses that result in crack propagation (e.g., Broek, 1982; Kanninen and Popelar, 1985), and the theory is appropriate for materials for which the region of plastic strain at the crack corners is small relative to the size of the crack.

In LEFM theory the material is assumed to be elastic, and three modes of fracture are defined, i.e., mode I (tension normal to the crack plane), mode II (sliding or displacement along the crack plane), and mode III (tearing or lateral displacement of the crack edges). The mode that is of interest to us is crack propagation through tension or specifically internal pressure, i.e., mode I.

For mode I, the generalized form of the equation describing the stress field near the tips of a crack of length $2a$ in an infinite plate is:

$$\sigma_{ij} = \frac{K_1}{2\pi r} f_{ij}(\theta) \text{ with } K_1 = \sigma(\pi a)^{1/2} \tag{7}$$

in which K_1 is the stress intensity factor, and σ is the tensile stress applied at infinity. The value r is radial distance from the crack tip, and θ is the angle relative to the plane of the crack (subscripts i and j are standard vector notation for summation over i and j). Once the magnitude of the stress intensity factor is known, the stress field is known. A parameter, K_{1c}, is defined as the critical stress intensity factor, a material property, and is the limit of K_1 at which the material fails. It is K_{1c} for sediments that will define bubble shape and bubble growth as a function of internal pressure. Consequently, the determination of K_{1c} is a primary objective of this study.

From Eq. 7, σ_{ij} goes to infinity as r goes to zero. This is an elastic response but, in reality, the stress does not go to infinity; rather, in the zone around the crack tip, there is plastic deformation. While the zone of plastic deformation is determined by the stress intensity factor and the yield stress, even with plastic deformation, K_1 is still a measure of all stresses and strains (Broek, 1984).

In practice, a plate with a crack of known size can be fractured through application of tensile stress. From the measured stress at failure, σ_c, the critical stress intensity factor, K_{1c}, can be calculated as:

$$K_{1c} = \sigma_c(\pi a_c)^{1/2} \tag{8}$$

This applies for the case in which a_c is small compared to the width of the plate.

In the analysis of the elastic-tip stress field, the stress intensity factor for a 'penny-shaped' crack of radius a imbedded in an infinite solid subjected to uniform tension is given as (Sneddon, 1946):

$$K_1 = \frac{2}{\pi}\sigma(\pi a)^{1/2} \tag{9}$$

By the principle of superposition, the equation for a 'penny-shaped' crack with internal pressure, P, is then:

$$K_1 = \frac{2}{\pi}P(\pi a)^{1/2} \tag{10}$$

and, at failure:

$$K_{1c} = \frac{2}{\pi}P_c(\pi a_c)^{1/2} \tag{11a}$$

in which the subscript 'c' is the critical value for crack propagation.

The expression for P_c is then:

$$P_c = \left(\frac{K_{1c}^2\pi}{4a_c}\right)^{1/2} \tag{11b}$$

In order to apply LEFM to data such as those in Fig. 3, we need to determine the critical pressure as a function of bubble volume. In LEFM theory, the crack-opening displacement, $\mathrm{COD}_{\max}$, may be described at the center line of the crack as: $\mathrm{COD}_{\max} = 4\sigma a/E$, in which E is Young's modulus. σ can be replaced by P_c for fracture to give:

$$(\mathrm{COD}_{\max})_c = \frac{4P_c a_c}{E} \tag{12}$$

Assuming an oblate spheroidal shape, in which $b = \mathrm{COD}/2$:

$$V = \frac{4}{3}\pi a^2 b \tag{13}$$

Expressing bubble volume as a function of P_c, then, from Eqs. 12 and 13):

$$V = \frac{16\pi a_c^3 P_c}{3E} \tag{14}$$

or solving for a_c:

$$a_c = \left[\frac{3EV}{8\pi P_c}\right]^{1/3} \tag{15}$$

Substituting Eq. 15 for a in Eq. 11b gives:

$$P_c = \frac{K_{1c}^{6/5} \pi^{4/5} (1/24)^{1/5}}{E^{1/5} V^{1/5}} \tag{16}$$

In Eq. 16, K_{1c} and E are constants, and thus, P_c is proportional to V to the $-1/5$ power. A log–log plot of P_c against V should then have a slope of $-1/5$ with an intercept, c, given by:

$$c = \log\left(\frac{1.32 K_{1c}^{6/5}}{E^{1/5}}\right) \tag{17}$$

in which again E is Young's modulus and K_{1c} is defined as the critical stress intensity factor, which is the limit of K_1 at which the material fails.

The troughs in the bubble growth data, e.g., Fig. 3, are also understandable in terms of LEFM (Green and Sneddon, 1950; Irwin, 1962; Broek, 1984). As gas is injected into the bubble, intuitively, one might expect that the critical pressure for a given bubble size would be reached, and then the bubble would grow at the critical pressure. However, in LEFM theory, kinetic energy of crack propagation is a component of the energy available for crack growth. Consequently, at the critical pressure, the crack grows, and then continues to grow at stresses below P_c until a level is reached at which crack growth is arrested. The theory of crack arrest is not as well developed as that for initiation, and we will not present more than this qualitative explanation here.

If our hypothesis that bubble growth occurs by fracture is true, then a log–log plot of the peak values of excess pressure, P_c (minus ambient pressure), in data such as those in Fig. 3 against bubble volume should be linear with a slope of $-1/5$. The value of K_{1c} can be calculated from Eq. 17. Note that the first peak, when the bubble forms initially, is not included as a value of P_c, because other factors such as capillarity and any blockage of the tip by sediment or interstitial water may contribute to its magnitude. Also, there is no reliable estimate of bubble volume at the time of this initial injection.

Which bubble volume results, i.e., from the volume perturbation or from constant PV, is the better predictor of the true bubble volume is not easily determined. As noted above, volume predicted by assuming constant PV is subject to errors from mass transfer, and bubble separation from the capillary. However, the volume perturbation method can be in error if, for example, each incremental addition of gas and concomitant pressure increase produces a small elastic response in the material. Fortunately, the volumes predicted by the two methods are generally within a factor of about 2. For bubble growth shown in Fig. 3, we will estimate the critical stress intensity factor, K_{1c}, using both methods.

Fig. 10 shows the log–log plot of excess pressure against predicted volume using the constant PV method for the data shown in Fig. 3. The best fit line from a regression of these data is also shown. Table 2 shows results for regression analyses for these data and for data obtained from gas injection into other sediment samples and into two samples of 2× gelatin. The results from the data of Fig. 3 show a slope that is essentially the predicted $-1/5$ power. The goodness of this fit and the apparent homogeneity of the region of the sample in which the bubble was injected are not typical of these sediments. Other injections into Cole Harbor samples typically gave results that either were of mixed types and could not be plotted as a series of peaks, or the regression fits were not as good. The results for 2× gelatin provided reasonably consistent regression fits that have slopes near $-1/5$, e.g., Table 2.

The difference in volumes determined by the two methods does not substantially affect the calculated values of K_{1c}. For the data in Fig. 3, the constant PV method gives a slope of -0.194 and an intercept of 1.220 while the volume perturbation method gives a slope of -0.20 and an intercept of 1.286. When transformed from logarithms the intercepts are 16.60 mbar cm$^{3/5}$ and 19.33 mbar cm$^{3/5}$, respectively. With these values of the intercepts and Young's modulus we can calculate K_{1c}.

Because Young's modulus (E) in Eq. 17 appears to only the 1/5 power, we initially assumed that values of E reported in the literature would be sufficient for calculation of K_{1c}. However, this assumption proved to be incorrect. We had some difficulty finding values of E in the literature, but

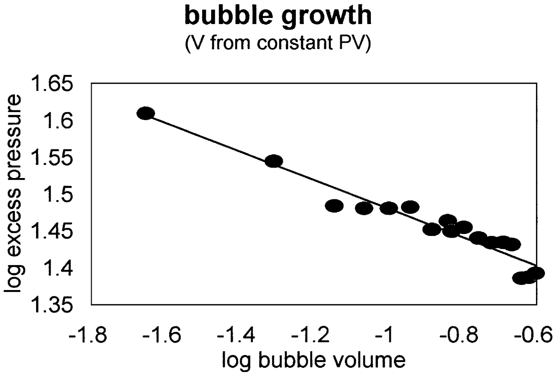

Fig. 10. Log–log plot for injection experiment for results shown in Fig. 3; sample mud 24:04:18. The best fit regression line is shown and the regression results described in Table 2.

one set of results, determined using acoustics for a range of sediment types by Raju and Ramana (1986), gave values for Young's modulus of between 2500 and 2900 MN m^{-2}. While we could calculate a value of K_{1c} using Eq. 16 and these reported results for E, we first tested to see if a reasonable COD$_{max}$ would result from these values of E using Eq. 12. Using an E of 2600 MN m^{-2} in Eq. 12 predicts that the crack opening displacement, COD$_{max}$, at the center of the bubble is ~0.1 μm. This result is not consistent with the shapes of bubbles determined from X-ray tomography for Eckernförde Bay samples, nor with our own X-ray images of bubbles injected into sediment samples, nor with visual results for injection of gas into gelatin. If COD$_{max}$ were 0.1 μm, injection of 0.3 ml of gas (a full injection in our method) would produce a bubble of 85 cm in radius – a size that clearly could not be contained in our sample. For injection of gas into gelatin, we estimated visually a width to height ratio of 0.03 to 0.09 for 2×gelatin and 1×gelatin samples, respectively, whereas, the width to height ratio using the Raju and Ramana (1986) value for E and the calculated COD$_{max}$ is ~10^{-7}. Furthermore, a value of E of 2600 MN m^{-2} substantially exceeds the reported Young's moduli for polyethylene at 10 MN m^{-2} and Nylon at 30 MN m^{-2}, two materials that we would intuitively expect to possess a Young's modulus higher than sediments.

The results of our determination of Young's modulus for Cole Harbor sediments, 0.139 MN m^{-2}, is more than four orders of magnitude less than the value determined acoustically by Raju

Table 2
Some results for regression analysis of critical pressure against bubble volume for gas injection experiments

Sample/experiment	Slope	Intercept	R^2	Details
Mud 24:04:18				
Constant *PV*	−0.194 (0.013)	1.286 (0.014)	0.936	
V perturbation	−0.200 (0.017)	1.220 (0.018)	0.905	
Mud 24:02:20				
Constant *PV*	−0.144 (0.012)	1.52 (0.013)	0.91	5 peaks
V perturbation	−0.191 (0.013)	1.43 (0.027)	0.90	
Mud 24:02:19				
Constant *PV*	−0.135 (0.048)	1.71 (0.0212)	0.57	8 peaks
V perturbation	−0.21 (0.050)	1.60 (0.016)	0.75	
Mud 24:01:19				
Constant *PV*	−0.09 (0.032)	1.83 (0.026)	0.67	6 peaks
V perturbation	−0.19 (0.061)	1.71 (0.029)	0.66	
2×Gelatin – 1				
Constant *PV*	−0.223 (0.028)	1.13 (0.031)	0.77	20 peaks
V perturbation	−0.183 (0.016)	1.23 (0.022)	0.88	
2×Gelatin – 2				
Constant *PV*	−0.202 (0.017)	1.22 (0.010)	0.90	18 peaks

For sediment samples, bubble volume was determined in two ways: by volume perturbation which involved injecting a known amount of gas and measuring the resulting pressure change, and by assuming the number of moles of gas and hence *PV* in the system remains constant during an experiment.

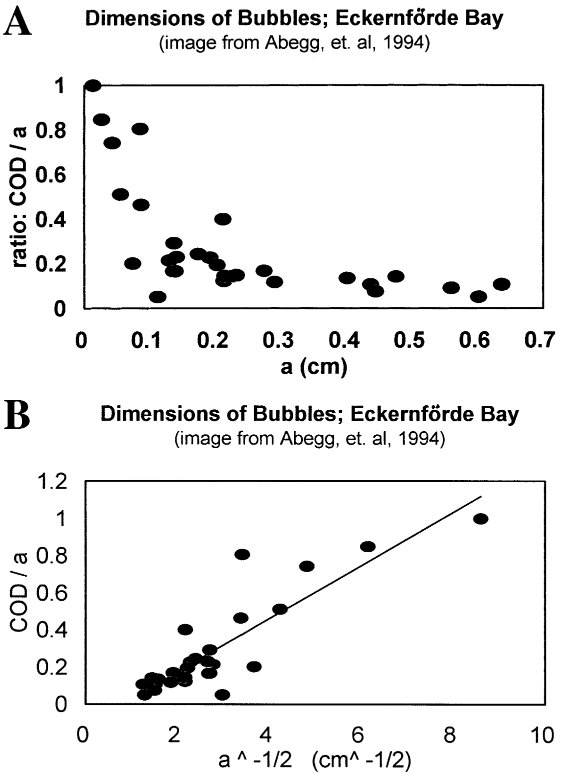

Fig. 11. Results for measurements of bubble sizes in the X-ray image of natural sediments at Eckernförde Bay (image from Abegg et al., 1994). (A) Ratio: ($\mathrm{COD_{max}}$) to a, versus a. (B) ($\mathrm{COD_{max}}$) to a, versus $a^{-1/2}$. The regression fit is also shown in B, featuring a slope of 0.143 (0.015); intercept of −0.113 (0.12) and $r^2 = 0.77$

and Ramana (1986). We do not know why this discrepancy exists. However, if we use our experimentally determined value for E in Eq. 12 we obtain a $\mathrm{COD_{max}}$ of 0.11 cm. This result gives a width to height ratio of ~0.05 when a is 1 cm, which is much closer to the results observed for bubbles injected in gelatin and for results for Eckernförde images.

Using 0.139 MN m^{-2} for Young's modulus and the regression results for P_c versus volume (determined both by the constant PV and volume perturbation methods) we obtain K_{1c} values of 2.8×10^{-4} MN m$^{-3/2}$ and 3.1×10^{-4} MN m$^{-3/2}$, respectively. We believe that these are the first results of this kind reported for natural sediment.

Estimates of K_{1c} can also be made from P_c and V for each peak in the pressure record of Fig. 3. Eq. 15 can be used to determine a_c, and then Eq. 11a used to calculate K_{1c}. From V determined by the volume perturbation method, the average K_{1c} for the results of Fig. 3 is 3.1×10^{-4} MN m$^{-3/2}$ with a standard deviation of 1.4×10^{-5} MN m$^{-3/2}$. This method gives the same estimate of K_{1c} as obtained from the intercept, but has the advantage in allowing estimates of K_{1c} to be made where fracture occurs in sediments that are not uniform, i.e., where the slope of the plot of log P_c versus log Vvaries from −1/5. In future work we plan to use this method to investigate the variability of K_{1c} in a range of sediment types.

An estimate of K_{1c} for the Eckernförde results can also be made. Fig. 11A shows the aspect ratio of bubbles plotted against bubble length determined for the X-ray tomography image presented by Abegg et al. (1994). The resulting plot shows that smaller bubbles tend to have a larger aspect ratio than do larger bubbles. Consequently, models of bubble growth that assume a spherical shape (Boudreau et al., 2002) better describe the growth of smaller bubbles. Solving Eq. 12 for P_c and substituting the result into Eq. 11b gives:

$$\mathrm{COD_{max}} = \frac{2(\pi a_c)^{1/2} K_{1c}}{E} \tag{18}$$

dividing both sides by a_c gives:

$$\frac{\mathrm{COD_{max}}}{a_c} = \frac{2\pi^{1/2}\, K_{1c}}{E a_c^{1/2}} \tag{19}$$

According to Eq. 18, a plot of ($\mathrm{COD_{max}}/a_c$) plotted against $a_c^{-1/2}$, should give a straight line with slope of $(2\pi^{1/2}\ K_{1c})/E$. This plot is shown in Fig. 11B along with the regression fit. From the slope determined by the regression and using E determined for the Cole Harbor sediments, the value of K_{1c} is determined to be 5.48×10^{-4} MN m$^{-3/2}$, or somewhat greater than determined for the Cole Harbor sediment sample. However, for the second Cole Harbor sample listed in Table 2, the K_{1c} values are 4.9×10^{-4} MN m$^{-3/2}$ and 4.1×10^{-4} MN m$^{-3/2}$ for constant PV and volume perturbation methods, respectively – results that are even closer to the Eckernförde estimate.

Bubble growth behavior by linear elastic fracture is fully determined by K_{1c}, Young's modulus and the rate of methane production. Using our methods and the results reported here, models can now be constructed to predict bubble growth rates in natural sediments.

The saw-tooth behavior is interpretable in terms of fracture, but the second type of observed growth behavior appears to fall between fracture and growth through a rheological mechanism. As demonstrated in the 1×gelatin, bubbles in this second mode of growth are disk-shaped, which is consistent with fracture, but grow at a relatively constant threshold pressure. In a future study we will further examine this mode of bubble growth behavior.

While gelatin is an excellent surrogate for visualizing bubble growth by fracture, its properties are somewhat different from those of sediments that we have studied. LEFM applies to materials for which the region of plastic deformation at the crack tips is small compared to the size of the fracture. In measurements of E for gelatin, $\Delta L/L$ was five times greater at the point of elastic failure than that determined for sediment samples. This fracture toughness was manifest in one set of experiments with gelatin in which we reduced the diameter of the cylinders for casting the samples. As bubbles grew in these smaller containers, the record of threshold pressures indicated that growth was increasingly influenced by the walls, even at distances from the wall as great as the bubble radius. Consequently, the region of plastic deformation at the crack tips for bubble growth in gelatin would need to be considered for a quantitative treatment of fracture.

5. Conclusions

We have studied the dynamics of bubble growth in sediments through injecting gas into natural core samples collected at Cole Harbor, NS. X-ray images (top view) of our samples (Fig. 2) show both natural bubbles and those injected to be crack-shaped and thus, consistent with those reported from X-ray tomography images of bubbles in natural samples (Abegg et al., 1994). In our studies, disk-shaped bubbles also formed when gas was injected into 1×gelatin and 2×gelatin, and showed the same growth behavior as many of our sediment samples.

Pressure was monitored during gas injection in order to determine stress and resulting strain that accompany bubble growth. Volumes of bubbles during injection of gas into sediment samples could not be determined visually, and bubble volume was thus inferred first by assuming constant PV and second through volume perturbation. This second method indicated changes in volume that may result from mass transfer or bubble separation from the capillary. The results of these two bubble volume determinations differed typically by less than a factor of 2.

The pressure–volume results show two types of growth behavior: (1) growth with pressure rising to a peak, signifying bubble formation, after which pressure rises and falls in a saw-tooth pattern as the bubble grows; and (2) pressure increase until bubble formation and then fall to a pressure intermediate between ambient starting pressure and the bubble formation pressure. The pressure then remains relatively constant during subsequent bubble growth. The first type of behavior and the disk shapes of the bubbles formed are consistent with a mechanism of growth by elastic fracture.

In order to analyze our results of bubble growth using the theory of linear elastic fracture mechanics (LEFM), it was necessary to measure Young's modulus for our sediments. Literature values of Young's modulus from acoustic determinations give unrealistic bubble shape estimates. Our results for Young's modulus are about four orders of magnitude lower than those reported in the literature and predict bubble shapes that agree well with observations.

Our results interpreted in terms of LEFM theory provide what we believe to be the first sediment values reported for the critical stress intensity factor, K_{1c}. The values of K_{1c} that we determined for Cole Harbor sediments range from $\sim 2.8\times10^{-4}$ MN m$^{-3/2}$ to $\sim 4.9\times10^{-4}$ MN m$^{-3/2}$. As a material property, K_{1c} is the parameter needed to understand bubble growth and the shapes of bubbles in sediments. As a further test of the theory, we have determined sizes of bubbles in X-ray tomography images from Eckernförde

Bay (Abegg et al., 1994), and have used the results with LEFM theory to predict a value of K_{1c} for sediments at that site. We obtained a K_{1c} of $\sim 5.5 \times 10^{-4}$ MN m$^{-3/2}$, a result that is only a little greater than the values of K_{1c} determined for Cole Harbor sediments.

Acknowledgements

We gratefully acknowledge support for this work by the US Office of Naval Research under Grant N00014-99-1-0063. The work also benefited from helpful discussions with Dr. Craig L. McNeil and Dr. Robert M. Gershey, and journal reviews by Aubrey L. Anderson and an anonymous reviewer.

Appendix A. Assessment of error in the perturbation method for determining bubble volume

In the perturbation method that we use the instantaneous bubble volume can be determined as long as the perturbation is large compared to the change in pressure due to mass transfer or temperature during the application of the perturbation. It is necessary to test the validity of this condition for our experiments.

This condition can be tested as follows.

In our experimental method:

$$P = f(VnT)$$

in which P, V, n, and T are the pressure, volume, number of moles and absolute temperature of the system, respectively, where the system refers to the bubble plus the injector and the connecting lines.

The total differential is:

$$\mathrm{d}P = \frac{\partial P}{\partial V}\mathrm{d}V + \frac{\partial P}{\partial n}\mathrm{d}n + \frac{\partial P}{\partial T}\mathrm{d}T \tag{A1}$$

Assuming applicability of the ideal gas law:

$$PV = nRT \tag{A2}$$

at constant T which is essentially true for our experiments (the effect of changing T will be tested below), Eq. A-1 becomes:

$$\frac{\mathrm{d}P}{\mathrm{d}V} = \frac{\partial P}{\partial V} + \left(\frac{\partial P}{\partial n}\right)\left(\frac{\mathrm{d}n}{\mathrm{d}V}\right) \tag{A3}$$

By the chain rule:

$$\left(\frac{\mathrm{d}P}{\mathrm{d}V}\right)\left(\frac{\mathrm{d}V}{\mathrm{d}t}\right) = \left(\frac{\partial P}{\partial V}\right)\left(\frac{\mathrm{d}V}{\mathrm{d}t}\right) + \left(\frac{\partial P}{\partial n}\right)\left(\frac{\mathrm{d}n}{\mathrm{d}V}\right)\left(\frac{\mathrm{d}V}{\mathrm{d}t}\right) \tag{A4}$$

and:

$$\left(\frac{\mathrm{d}P}{\mathrm{d}t}\right) = \left(\frac{\partial P}{\partial V}\right)\left(\frac{\mathrm{d}V}{\mathrm{d}t}\right) + \left(\frac{\partial P}{\partial n}\right)\left(\frac{\mathrm{d}n}{\mathrm{d}t}\right) \tag{A5}$$

From the ideal gas law the partial differential terms can be determined to give:

$$\left(\frac{\mathrm{d}P}{\mathrm{d}t}\right) = \left(\frac{-nRT}{V^2}\right)\left(\frac{\mathrm{d}V}{\mathrm{d}t}\right) + \left(\frac{RT}{V}\right)\left(\frac{\mathrm{d}n}{\mathrm{d}t}\right) \tag{A6}$$

and since (nRT/V) is equal to P:

$$\left(\frac{\mathrm{d}P}{\mathrm{d}t}\right) = \left(\frac{-P}{V}\right)\left(\frac{\mathrm{d}V}{\mathrm{d}t}\right) + \left(\frac{RT}{V}\right)\left(\frac{\mathrm{d}n}{\mathrm{d}t}\right) \tag{A7}$$

The first term on the right describes the change in pressure due to the combined effects of activation of the piston (decrease in volume in the system, i.e., the volume perturbation) plus mass transfer (diffusive loss). The second term provides change in pressure due to mass transfer only. For the perturbation method to work:

$$\left[\frac{-P}{V}\frac{\mathrm{d}V}{\mathrm{d}t}\right] \gg \left[\frac{RT}{V}\frac{\mathrm{d}n}{\mathrm{d}t}\right] \tag{A8}$$

which can only be valid if the mass transfer effect on pressure is much smaller than the effect of perturbing the volume. Note that square brackets mean absolute values.

Reference to Fig. 3 and Fig. A1 demonstrates the relative importance of mass transfer and volume perturbation in the pressure response. Note that in Fig. 3 the pressure rises in a series of small steps that are the volume perturbations resulting from activation of the piston of the injection system. When the stress reaches the fracture point, the pressure falls as the bubble grows, creating the saw-tooth pattern of the figure. We are using the

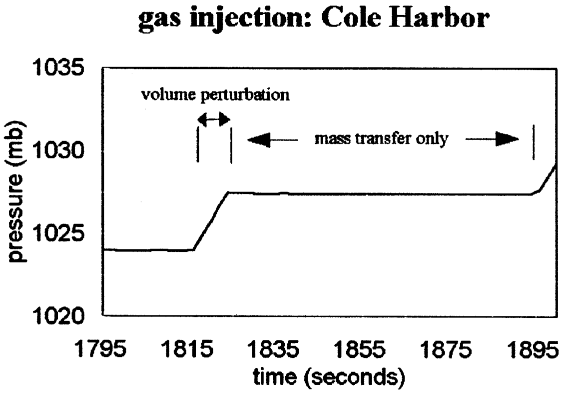

Fig. A1. Typical pressure response to a single volume perturbation in which bubble growth does not occur (taken from the experimental results shown in Fig. 3).

steps in pressure *that do not result in bubble growth* to determine system volume. Bubble growth when fracture occurs is readily identified because there is a kinetic component to the process, which causes the pressure to fall well below the threshold stress.

A pressure response from a typical volume perturbation resulting from piston activation is shown in Fig. A1. In that figure, the pressure change from the volume perturbation (plus mass transfer) is considerably greater than the ensuing change due to mass transfer alone. In fact, the average of 10 steps chosen at random from the results of the experiment gave a [dP/dt] for the volume perturbation of 0.385 mbar/s, compared to an average [dP/dt] of 0.00132 mbar/s during the ensuing 10 periods of mass transfer alone. The factor of about 300 difference means that the effect of mass transfer and hence the second term in Eq. 7 above is negligible during the period of the volume perturbation.

Concerning the effect of a changing temperature on our experimental results, we note that the appropriate term for Eq. 7 would be (P/T) (dT/dt). At a pressure of 1020 mbar, and room temperature of 293 K, a temperature change of 1 K over the period of the experiment shown in Fig. 3 would provide a pressure change contribution of ~0.0005 mbar/s. A temperature change of 2 K, which is the maximum we would expect during the course of an experiment, would give a change comparable to that from mass transfer, and the two combined are then still insignificant compared to the volume perturbation.

Appendix B. Assessment of the contribution of capillary pressure

In studies involving injection of gas into a liquid medium the role of capillary pressure (also known as Laplace or surface tension pressure) needs to be assessed. As indicated previously, the first peak in the record of bubble pressure shown in Fig. 3 has not been interpreted in terms of the critical pressure for fracture, because this peak represents the pressure when the bubble first forms at the capillary tip. Once the bubble is formed, a component of its internal pressure is due to surface tension, i.e., capillary pressure.

For a spherical bubble the capillary pressure is $p_c = 2\gamma/r$, in which γ is surface tension and r is spherical bubble radius. For the smallest bubble that forms in our study, i.e., just after formation at the capillary tip and with size estimated by the volume perturbation method, the bubble volume is 0.015 cm^3 with a spherical radius of 0.15 cm. Assuming a surface tension of 0.072 N m^{-1}, this size of bubble has a capillary pressure of 0.96 mbar. If this bubble is then distorted to oblate spheroid shape at constant volume the capillary pressure can be estimated from:

$$p_c = \gamma\left(\frac{1}{r_1}+\frac{1}{r_2}\right) \tag{B1}$$

in which r_1 and r_2 are the major and minor axes.

For a bubble of 0.015 cm^3 in our studies we can determine r_1 and r_2 from Eqs. 12 and 15 as 0.398 cm and 0.023 cm, respectively. From Eq. B-1) the capillary pressure is 3.39 mbar. This excess capillary pressure, i.e., the difference between the capillary pressure of the oblate spheroid and the capillary pressure of an equivalent sphere (3.39–0.96 mbar or 2.35 mbar) is part of the stress exerted by the bubble on the surrounding sediment, and contributes to fracture as part of P_c. The capillary pressure associated with the equivalent spherical bubble is an error in our method, because it is also a contributor to P_c without contributing to the stress that leads to fracture, i.e., it is an enhancement of internal pressure that results from surface tension. This error is only ~2.5% of P_c and, as such, is smaller than the error due to uncertainty in the bubble volume.

References

Abegg, F., Anderson, A., Buzi, L., Lyons A.P., Orsi, T.H., 1994. Free methane concentration and bubble characteristics in Eckernförde Bay, Germany. In: Wever, T.F. (Ed.), Forschungsanstalt der Bundeswehr für Wasserschall- und Geophysik (FWG), Bonn, pp. 84–89.

Boudreau, B.P., Gardiner, B.S., Johnson, B.D., 2002. Rate of growth of isolated bubbles in sediments with a distributed source of methane. Limnol. Oceanogr., 46, 616–622.

Broek, D., 1984. Elementary Engineering Fracture Mechanics. Martinus Nijhoff, Boston, MA, 469 pp.

Chanton, J.P., Martens, C.S., Kelley, C.A., 1989. Gas transport from methane-saturated, tidal freshwater and wetland sediments. Limnol. Oceanogr. 34, 807–819.

Crill, P.M., Harris R.C., Bartlett, K.B., 1991. Methane fluxes from terrestrial wetland environments. In: Rogers, J.E., Whitman, W.B. (Eds.), Microbial Production and Consumption of Greenhouse Gases: Methane, Nitrogen Oxides, and Halomethanes. Am. Soc. Microbiol., Washington, DC, pp. 91–109.

Green, A.E., Sneddon, I.N., 1950. The stress distribution in the neighborhood of a flat elliptical crack in an elastic solid. Proc. Cambridge Phil. Soc. 46, 159–164.

Irwin, G.R., 1962. The crack extension force for part-through crack in a plate. Trans. ASME J. Appl. Mech. 651–654.

Judd, A.G., Hovland, M., 1992. The evidence of shallow gas in marine sediments. Cont. Shelf Res. 12, 1081–1095.

Kanninen, M.F., Popelar, C.H., 1985. Advanced Fracture Mechanics. Oxford University Press, New York, 563 pp.

Martens, C.S., Berner, R.A., 1974. Methane production in the interstitial waters of sulfate-depleted marine sediments. Science 185, 1167–1169.

Martens, C.S., Klump, J.V., 1980. Biogeochemical cycling in an organic rich coastal marine basin. I. Methane sediment–water exchange processes. Geochim. Cosmochim. Acta 44, 471–490.

Raju, L.V., Ramana, Y.V., 1986. Physical and elastic properties of marine sediments off Bombay. Indian Mar. Geotechnol. 6, 359–375.

Sneddon, I.N., 1946. The distribution of stress in the neighborhood of a crack in an elastic solid. Proc. R. Soc. London Ser. A 187, 229–260.

Strayer, R.F., Tiedje, J.M., 1978. In situ methane production in a small, hypereutrophic, hard-water lake: loss of methane from sediments by vertical diffusion and ebullition. Limnol. Oceanogr. 23, 1201–1206.

Wheeler, S.J., 1988. The undrained shear strength of soils containing large gas bubbles. Géotechnique 38, 399–413.